






# Observation of resonant spin excitation with in-plane spin wave propagation in hybrid antiskyrmion strings

Daisuke Nakamura <sup>1,\*</sup>, Kosuke Karube,<sup>1</sup> Yizhou Liu <sup>1</sup>, Fumitaka Kagawa,<sup>1,2</sup> Xiuzhen Yu <sup>1</sup>,  
Yoshinori Tokura <sup>1,3</sup> and Yasujiro Taguchi <sup>1</sup>

<sup>1</sup>*RIKEN Center for Emergent Matter Science (CEMS), Wako 351-0198, Japan*

<sup>2</sup>*Department of Physics, Tokyo Institute of Technology, Tokyo 152-8551, Japan*

<sup>3</sup>*Tokyo College and Department of Applied Physics, University of Tokyo, Tokyo 113-8656, Japan*



(Received 14 January 2024; revised 24 April 2024; accepted 5 June 2024; published 12 July 2024)

Topological magnetic textures provide a rich variety of collective excitations. We report microwave resonant dynamics of hybrid antiskyrmion strings in a microfabricated thin plate of  $(\text{Fe}_{0.60}\text{Ni}_{0.32}\text{Pd}_{0.08})_3\text{P}$  at 300 K. With the aid of a micromagnetic simulation, the observed resonant peaks are identified as gyrotropic motions of hybrid antiskyrmions. The simulation reveals that the magnetization dynamics at the singularity points (Bloch points) in the hybrid antiskyrmions induces in-plane propagation of a spin wave, highlighting the internal structure as an important difference from skyrmions.

DOI: [10.1103/PhysRevB.110.024418](https://doi.org/10.1103/PhysRevB.110.024418)

## I. INTRODUCTION

Topological magnetic textures have recently attracted much attention as they give rise to various interesting phenomena [1–4], such as topological Hall and Nernst effects. A representative example of the topological textures is the skyrmion with a spin-swirling structure, which can be regarded as a stable particle and driven by a low current density. Due to this feature, the skyrmion is anticipated to be applied to spintronic devices. Another example is the antiskyrmion that possesses a topological charge [1] of  $Q_t = 1$  with an opposite sign to the skyrmion ( $Q_t = -1$ ), where  $Q_t = \frac{1}{4\pi} \int \vec{m} \cdot (\frac{\partial \vec{m}}{\partial x} \times \frac{\partial \vec{m}}{\partial y}) dx dy$ , and  $\vec{m}$  is the normalized magnetization vector.

The skyrmion emerges due to the Dzyaloshinskii-Moriya (DM) interaction [5] in chiral [6] or polar magnets [7] and to the frustrated exchange interaction [8] in centrosymmetric magnets. On the other hand, the antiskyrmion is stabilized by a dipolar interaction [9,10] together with an anisotropic DM interaction [11,12]. Figure 1(a) shows a schematic magnetization configuration in antiskyrmion strings, which consist of four Bloch-type walls and four Néel-type walls at the intersections, the latter of which are regarded as defects of the Bloch-type walls, and hence called Bloch lines. Due to the dominance of the dipolar interaction in contrast to the case of DM-induced chiral skyrmions, the lateral size of an antiskyrmion and the corresponding lattice constant of the periodic structure can be tuned with the length of an antiskyrmion string,  $L_z$ . Experimentally, antiskyrmions have thus far been observed in  $\text{Mn}_{1.4}\text{Pt}_{0.9}\text{Pd}_{0.1}\text{Sn}$  with  $D_{2d}$  symmetry [13],  $(\text{Fe}_{0.63}\text{Ni}_{0.30}\text{Pd}_{0.07})_3\text{P}$  with  $S_4$  symmetry [14], and ferrimagnetic multilayers [15].

The dynamics of the topological magnetic textures excited by dc electrical current has been investigated, and current-driven skyrmions with a low threshold density [16] as well as the skyrmion Hall effect [17,18] have been observed. As for ac stimuli, a microwave excitation can drive resonant dynamics of the topological magnetic textures that manifests itself as a characteristic absorption spectrum, thereby providing a novel high-frequency functionality. In a skyrmion system, gyrotropic motions with clockwise (CW) and counterclockwise rotations are excited by the in-plane oscillation of an external magnetic field, whereas a breathing motion is induced by the out-of-plane excitation [19]. There have been experimental reports for the observation of such resonant modes in skyrmion materials [20–36]. On the other hand, the resonant dynamics for the antiskyrmion has not yet been observed experimentally, while similar gyrotropic and breathing modes are predicted in the previous numerical calculations for extremely thin antiskyrmions [10,11,37] with a circular shape like the skyrmions. In the actual materials, antiskyrmions with  $L_z = 200 - 1000$  nm in  $(\text{Fe}, \text{Ni}, \text{Pd})_3\text{P}$  exhibit a square-rod shape at room temperature [38] as depicted in Fig. 1(a) due to the significant effect of the dipolar interaction. In addition, the three-dimensional magnetic domain structure in bulk  $(\text{Fe}, \text{Ni}, \text{Pd})_3\text{P}$  has been reported to be complex due to the competition of the exchange, anisotropic DM, uniaxial anisotropy, and demagnetization energies, resulting in the sawtoothlike domain pattern near the bulk surfaces [14]. For the thin plate, an antiskyrmion string with a Néel-skyrmion-like surface layer is expected, since the magnetic flux near the surface tends to form a closure loop. Such a hybrid antiskyrmion string accompanies singularity points of magnetization (called Bloch points) at the interface between the surface Néel-skyrmion-like layer ( $Q_t = -1$ ) and bulk antiskyrmion layer ( $Q_t = 1$ ), and has recently been observed by a holographic vector-field electron tomography in  $(\text{Fe}, \text{Ni}, \text{Pd})_3\text{P}$  [39]. Since the resonant dynamics should be

\*Contact author: daisuke.nakamura.rg@riken.jp

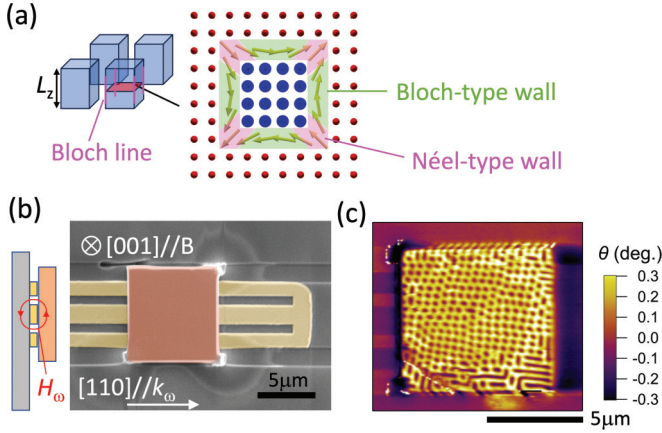


FIG. 1. (a) Light-blue pillars in the left panel represent a square lattice of antiskyrmions. Four edges in an antiskyrmion rod colored in pink represent Bloch lines. Right panel shows the schematic magnetization configuration at the middle of the antiskyrmion rod with the length of  $L_z$ . The hatched regions in green and pink indicate the Bloch-type and Néel-type walls, respectively. Large blue (small red) dots represent the magnetizations pointing down (up). (b) A scanning electron microscopy image of an  $(\text{Fe}_{0.60}\text{Ni}_{0.32}\text{Pd}_{0.08})_3\text{P}$  thin plate (pink) on the coplanar waveguide (yellow). The left schematic view illustrates the cross section of the coplanar waveguide and the distribution of the magnetic field component of a microwave ( $H_\omega$ ) transmitted along the waveguide. (c) Magnetic force microscopy image of the thin plate, captured at 298 K after the field-cooling process at 50 mT from 400 K. In (b) and (c), black scale bars represent 5  $\mu\text{m}$ .

largely affected by the magnetic interaction in the topological magnetic textures as well as by their sizes, density, and internal structure, it is worth investigating how the hybrid antiskyrmion strings respond to microwave excitations.

In this work, we reveal the resonant modes of metastable hybrid antiskyrmion strings created in a microfabricated plate of  $(\text{Fe}, \text{Ni}, \text{Pd})_3\text{P}$ . Microwave absorption peaks are observed and assigned to the gyrotropic modes with the help of micro-magnetic simulation. The numerical analysis of the resonant modes suggests that the observed gyrotropic motion is accompanied by an in-plane spin wave propagation along the Bloch-type walls of hybrid antiskyrmion strings, which is triggered by the singularity points, namely, the Bloch points, within the Bloch lines.

## II. EXPERIMENT

A single crystal of  $(\text{Fe}_{0.60}\text{Ni}_{0.32}\text{Pd}_{0.08})_3\text{P}$  was grown by the self-flux method, whose details were described elsewhere [40]. The thin-plate sample with 8  $\mu\text{m}$  in lateral size and 0.54  $\mu\text{m}$  in thickness was fabricated by using a focused ion beam (FIB) instrument (Helios 5 UX, Thermo Fisher Scientific and NB-5000, Hitachi), and was attached on top of the coplanar waveguide, with  $[110]$  parallel to the Poynting vector of the microwave as shown in Fig. 1(b). The excitation magnetic field  $H_\omega$  acts as the in-plane excitation on the magnetic textures. The coplanar waveguide is made of 150-nm-thick gold patterned on a  $\text{SiO}_2(300\text{nm})/\text{Si}$  substrate by using a maskless UV photolithography system (D-light-DL1000RS, Nano Systems Solutions) and an electron beam heating

evaporation system (EB-evap, Katagiri Engineering). Tiny burrs at the edge of gold electrodes created unintentionally by the liftoff process were removed by the FIB milling, to avoid tilting of an  $(\text{Fe}, \text{Ni}, \text{Pd})_3\text{P}$  thin plate put on the electrodes. Then, an  $\text{Al}_2\text{O}_3$  layer with 30 nm thickness was deposited to cover the gold electrodes. The measurement sample was fixed on an  $\text{Al}_2\text{O}_3$  layer by depositing Pt in the FIB chamber. The chemical composition of the thin plate used in this work was evaluated to be  $(\text{Fe}_{0.60}\text{Ni}_{0.32}\text{Pd}_{0.08})_3\text{P}$  by using energy dispersive x-ray spectroscopy.

A square lattice of metastable hybrid antiskyrmions were created by a field-cooling process [38] with 50 mT from 400 K, then the magnetic field was reduced to zero at 300 K (Fig. S1 in the Supplemental Material [41]). The emergence of a square lattice of hybrid antiskyrmions was confirmed prior to the magnetic resonance experiments as shown in Fig. 1(c) (also see Fig. S2 in the Supplemental Material [41]) by magnetic force microscopy (MFM) using a scanning probe microscope (MFP-3D, Asylum Research) and an MFM cantilever (MFM, Nano World) at ambient temperature, typically 298 K. Then, for the magnetic resonance experiment, a reflection coefficient of a microwave ( $S_{11}$ ) spectrum up to 20 GHz was measured by a network analyzer (N5224A, Agilent), in the field-up-sweep and subsequent field-down-sweep runs, respectively. In Sec. III, we show only the result for the up-sweep measurement ( $S_{11,\text{up}}$ ). The result of the down-sweep measurement ( $S_{11,\text{down}}$ ) is described in the Supplemental Material [41] (Sec. C). We prepared a pair of coplanar waveguides with the same dimension just next to each other on a single substrate, and the microfabricated plate of  $(\text{Fe}, \text{Ni}, \text{Pd})_3\text{P}$  was set on one of the pair waveguides. The other waveguide was used as a reference. The  $S_{11}$  signal of the reference was subtracted from that of the sample and plotted in Sec. III A. All measurements were performed at 300 K. Details are described in the Supplemental Material [41].

## III. RESULTS AND DISCUSSIONS

### A. Magnetic-field dependent resonant peaks at 300 K

In a magnetic resonance experiment, the  $S_{11}$  spectrum is measured in a field-up-sweep run after creating the metastable hybrid antiskyrmion lattice. As shown in Fig. 2(a), a resonant feature is observed at 7 GHz under zero magnetic field, whose resonant frequency gradually decreases with increasing the external magnetic field. The lateral size of hybrid antiskyrmions also decreases gradually with increasing the magnetic field in  $(\text{Fe}, \text{Ni}, \text{Pd})_3\text{P}$  [Ref. [38]; see also Supplemental Material [41], Fig. S8(a)], which may be relevant to the field-induced monotonous evolution of the resonant frequency. Around 0.32 T, the resonant peak shows a small discontinuity (see Supplemental Material [41], Fig. S4 for details). We also observe a somewhat blurred but discernible resonant feature around 12 GHz under zero field, whose frequency increases as the field is increased. In the forced single-domain ferromagnetic state above 0.42 T ( $B_c$ , blue dotted line), a  $B$ -linear ferromagnetic resonance mode (Kittel mode) is observed. We also find a small side peak of the Kittel mode at a slightly lower frequency, which is attributed to the standing spin wave resonance across the thickness direction of

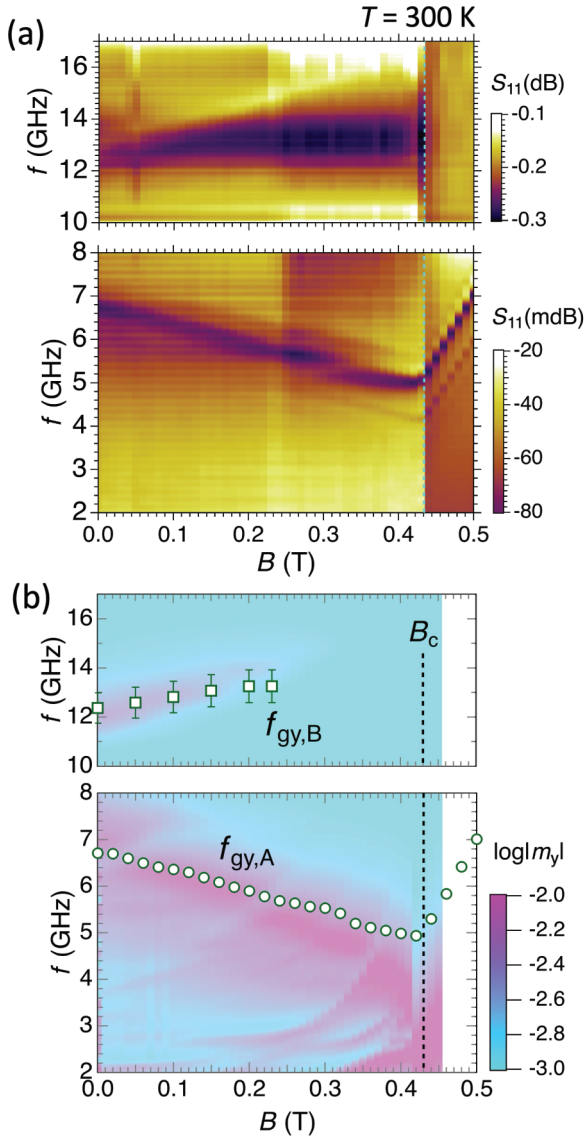


FIG. 2. (a) Magnetic field evolution of the  $S_{11}$  spectrum for the field-up-sweep run of the magnetic resonance experiment at 300 K. The vertical dashed line indicates the transition field into the forced single-domain ferromagnetic state,  $B_c$ . Metastable hybrid antiskyrmions are created by the field cooling before the experiment. Above  $B_c$ , a constant offset is added to  $S_{11}(f, B)$  to make a clearer view. (b) Magnetic field dependence of the resonant frequencies, which are determined from (a), and depicted as open symbols. For comparison, the FFT amplitude of spatially averaged in-plane magnetization ( $m_y$ ) calculated by the micromagnetic simulation (also see Fig. S8 of the Supplemental Material [41]) is also shown as the color map. The resonant modes corresponding to the experiment turn out to be gyrotropic modes, and are labeled as  $f_{gy,A}$  and  $f_{gy,B}$ , respectively.

the thin plate [31]. The continuous evolution of the resonant frequency across  $B_c$  implies that the lateral size of magnetic textures below  $B_c$  gradually shrink and disappear to form the single-domain ferromagnetic state upon increasing the magnetic field, in accord with our previous report [42].

In Fig. 2(b), we summarize the magnetic field evolution of the resonant frequencies observed in Fig. 2(a). We also

overlay the color map of the fast Fourier-transformed frequency spectra of the spatially averaged in-plane magnetization,  $m_y$ , depicting the field evolution of the resonant spectra of hybrid antiskyrmions obtained by our micromagnetic simulation. Micromagnetic simulation was performed by using MUMAX3 [43]. Four hybrid antiskyrmions forming a cluster with a square shape were investigated by minimizing the following energy functional:

$$E(\vec{m}) = \int_V \left\{ A_{\text{ex}} (\nabla \vec{m})^2 + D [\vec{m} \cdot (\vec{e}_x \times \partial_x \vec{m}) - \vec{m} \cdot (\vec{e}_y \times \partial_y \vec{m})] - K_u (\vec{m} \cdot \vec{e}_z)^2 - \frac{M_s}{2} \vec{m} \cdot \vec{B}_d - M_s \vec{m} \cdot \vec{B}_{\text{ext}} \right\} dV,$$

where  $A_{\text{ex}}$  is the exchange stiffness,  $\vec{m}$  is the normalized magnetization,  $D$  is the DM interaction constant,  $K_u$  is uniaxial anisotropy,  $\vec{e}_{x,y,z}$  is the unit vector along the  $x$ ,  $y$ , and  $z$  directions,  $M_s$  is the saturation magnetization,  $\vec{B}_d$  is the demagnetizing field,  $\vec{B}_{\text{ext}}$  is the external field, and  $V$  is the volume of the thin plate. We took into account the anisotropic DM interaction ( $D_x = -D_y$ ), similarly to Ref. [14]. The parameters used in the simulation are based on those experimentally evaluated at 300 K in the previous reports [14,40];  $A_{\text{ex}} = 8.1$  pJ/m,  $D = 0.2$  mJ/m<sup>2</sup>,  $M_s = 540$  kA/m, and  $K_u = 31$  kJ/m<sup>3</sup>. We do not consider the effect of thermal fluctuation. The excitation magnetic field of  $B_0 \text{sinc}[2\pi f_0(t - t_0)] = B_0 \sin[2\pi f_0(t - t_0)]/[2\pi f_0(t - t_0)]$  ( $B_0 = 0.5$  mT,  $f_0 = 100$  GHz, and  $t_0 = 0.01$  ns) was applied along the in-plane ( $y$ ) direction to excite various types of resonant modes. The temporal response of spatially averaged magnetization was converted to the frequency spectrum by fast Fourier transformation (FFT).

In Fig. 2(b), two peaks ( $f_{gy,A}$  and  $f_{gy,B}$ ) are clearly discerned at 6.9 and 12.0 GHz at zero field. The simulated frequency values as well as their field dependencies well coincide with those of the experimentally observed modes. Above 0.2 T, the simulated resonant frequency becomes slightly lower than the experiment, which might be caused by a change in the density of the textures in the experiment. By comparing the simulation result with the experimental data, we identify the observed resonant modes as the gyrotropic modes  $f_{gy,A}$  and  $f_{gy,B}$ , as explained in detail in Sec. E of the Supplemental Material [41]. The resonant modes with lower frequencies than  $f_{gy,A}$  are not observed in the experiment shown in Fig. 2(a), probably due to high reflectivity for the microwave at the surface as well as to the surface-layer-dominant feature of the low-frequency resonant modes, which is explained in the Supplemental Material [41] (Sec. E). Other components of the simulated magnetization are described in Supplemental Material [41], Fig. S8.

The observed jumplike spectral feature of the resonant frequency around 0.32 T may be attributed either to the transformation from hybrid antiskyrmions to nontopological bubbles or skyrmions observed in a thinner plate [38], or to the hybridization with higher-order resonant modes as observed in Cu<sub>2</sub>OSeO<sub>3</sub> [32]. According to our preliminary simulation result, the resonant modes of nontopological bubbles or skyrmions appear to have slightly larger frequencies (not shown), contrary to the experiment. On the other hand, the hybridization of the  $f_{gy,A}$  mode with higher-order resonant modes is predicted to take place under the magnetic fields



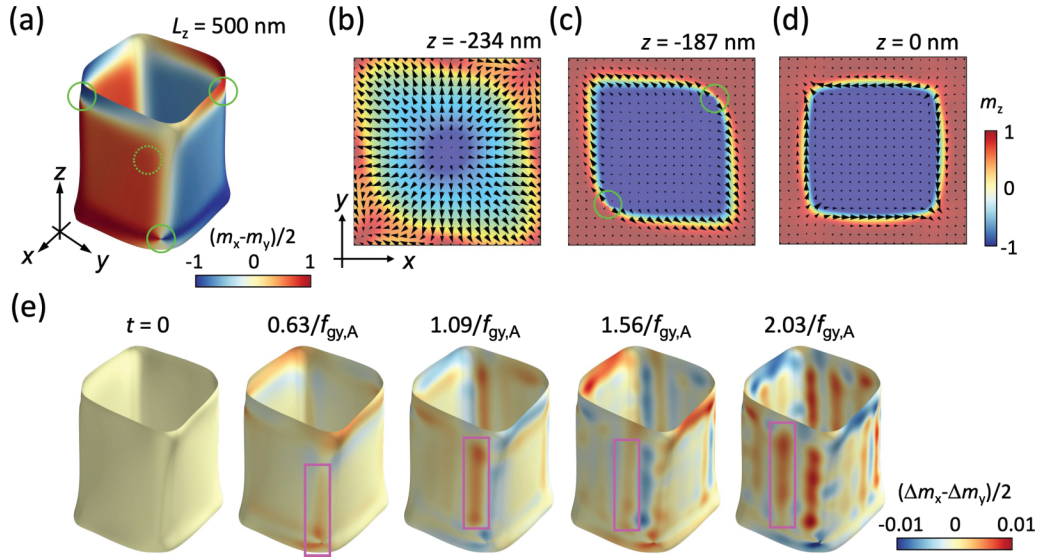


FIG. 3. (a) 3D view of a hybrid antiskyrmion rod with the length ( $L_z$ ) of 500 nm. The isosurface of  $m_z(x, y, z) = 0$  is depicted as the wall of the hybrid antiskyrmion, and  $(m_x - m_y)/2$  value on the isosurface is presented as the color map. (b)–(d) In-plane cross-sectional views of the hybrid antiskyrmion rod at different  $z$  positions. The color code and the black arrows represent  $m_z$  and the in-plane magnetization component, respectively. The drawing area is 500 nm square. The  $z$  positions ( $-250 \text{ nm} < z < 250 \text{ nm}$ ) from the center of the string are (b)  $-234 \text{ nm}$  (close to the bottom surface), (c)  $-187 \text{ nm}$ , and (d)  $0 \text{ nm}$ , respectively. In (a) and (c), the positions of the Bloch points are indicated by green circles. The dotted green circle in (a) indicates the Bloch point hidden at the back of the front wall of the hybrid antiskyrmion string. (e) Temporal change of in-plane magnetization,  $(m_x - m_y)/2$ , on the wall of a selected single hybrid antiskyrmion string for the gyrotropic A ( $f_{\text{gy,A}}$ ) mode. To highlight a tiny change in  $(m_x - m_y)/2$ , the value at  $t = 0$  is subtracted as a background, and 3D views at selected times are plotted. The pink square regions at  $t = 0.63/f_{\text{gy,A}} - 2.03/f_{\text{gy,A}}$  represent the propagation of spin wave along the in-plane direction.

while the observed experimental feature is too vague to be unambiguously identified as such a mode hybridization within our current experimental sensitivity.

### B. In-plane propagation of spin wave accompanied by gyrotropic motion of hybrid antiskyrmons

Next, we analyze the dynamics of the  $f_{\text{gy,A}}$  mode in more detail, which is related to the complex three-dimensional structure of the hybrid antiskyrmion strings. It should be noted that the wall structure of the hybrid antiskyrmion string qualitatively changes with the  $z$  position along the string. Figure 3(a) displays the isosurface of  $m_z(x, y, z) = 0$ , which represents the wall of the hybrid antiskyrmion string with  $L_z = 500 \text{ nm}$ . On the isosurface,  $(m_x - m_y)/2$  is plotted as a color map, and there are four singularity points (Bloch points, as indicated by the green circles) within the Bloch lines. Two Bloch points are located near the top surface and the other two are close to the bottom surface of the hybrid antiskyrmion string. Recently, the Bloch point has been observed as the termination point or the saddle point of the string of topological magnetic texture [44–46]. The Bloch points discussed in this work and Ref. [39] are the topological defects within the Bloch lines.

The magnetic textures above and below the Bloch points are qualitatively different from each other. Figures 3(b)–3(d) depict the in-plane cross-sectional views of the hybrid antiskyrmion at  $z = -234$ ,  $-187$ , and  $0 \text{ nm}$ , relative to the center of the string with a total length of  $L_z = 500 \text{ nm}$ . At  $z = -187 \text{ nm}$  [Fig. 3(c)], two Bloch points (green circles) are

observed at the top-right and bottom-left corners of the wall. Below the Bloch points [Fig. 3(b)], the in-plane magnetization vectors point outward from the center and exhibit a Néel-skyrmion-like texture, due to the formation of the flux-closure loop near the surface. On the other hand, the antiskyrmion-type texture is observed above the Bloch points [Fig. 3(d)]. Additionally, it is worth noting that when  $L_z$  is reduced to 100 nm, no Bloch points emerge on the wall of the antiskyrmion in the simulation (see Supplemental Material [41], Fig. S5). This is because the energy cost associated with the creation of the Bloch points exceeds the magnetostatic-energy gain by the formation of the Néel-skyrmion-like layer with reduced surface magnetic charge.

To visualize the evolution of in-plane magnetization on the wall including those at the Bloch points and Bloch lines, the excitation magnetic field of  $B_0 \sin(2\pi f_{\text{gy,A}} t)$  was applied and the temporal change of the magnetization is displayed in Fig. 3(e). At  $t = 0.63/f_{\text{gy,A}}$ , the in-plane magnetization becomes apparent at the Bloch points and the Néel-skyrmion-like surface layer. Then, at  $t = 1.09/f_{\text{gy,A}}$ , a vertical red part evolves from the Bloch point and moves away from the corner of the hybrid antiskyrmion, namely, the Bloch line. This vertical part propagates along the lateral direction of the wall as a spin wave. Almost one cycle later in  $H_\omega(t)$  ( $t = 2.03/f_{\text{gy,A}}$ ), a new vertical red pattern appears at the Bloch line. Magnetization dynamics within the surface layer ( $|z| > 187 \text{ nm}$ ) is distinct from the propagating spin wave, as exemplified by the different colors between the surface layer and the bulk layer ( $|z| < 187 \text{ nm}$ ) at  $t = 2.03/f_{\text{gy,A}}$ . This induces the standing-wave-like behavior of the spin wave along the out-of-plane

direction for the bulk layer. The motion of the pink square region in Fig. 3(e) indicates a speed of 0.58 km/s of the in-plane propagation.

This spin wave propagates along the wall and in a perpendicular direction to the hybrid antiskyrmion string, and hence differs from the out-of-plane propagation along a skyrmion string, as observed in  $\text{Cu}_2\text{OSeO}_3$  [33]. The propagation direction is CW as viewed from the  $+z$  direction, irrespective of the direction of the gyrotropic motion of the core (see Supplemental Material [41] videos B and C), and governed by the direction of core magnetization. The temporal evolution of magnetization at the Bloch points and Bloch lines (as a wall separating the adjacent Bloch walls) shown in Fig. 3(e) indicates that the key ingredient can be the existence of these singularities in the hybrid antiskyrmion string. A similar phenomenon is predicted in a Permalloy thin film [47]; a spin wave is generated from the Bloch-point-like singularity point and the domain wall (corresponding to the Bloch line in this work) by the microwave excitation, and propagates perpendicular to the domain wall.

In Fig. 3(e), the magnetization around the Bloch point responds to the microwave excitation prior to that of the Bloch line (see also Supplemental Material [41], video B). This possibly indicates high sensitivity of the Bloch point against the disturbance for the following reason. In the framework of the Landau-Lifshitz-Gilbert equation describing the dynamics of magnetization, the effective field acting on a spin can be decomposed into the exchange field from the adjacent spins, the longer-ranged dipolar field from the farther spins, and the

external field (microwave in this case). Around the center of the Bloch point texture, the exchange and the dipolar fields can be negligible due to cancellation. As a result, the external field (microwave) provides a relatively large influence on the magnetization dynamics at the Bloch points.

#### IV. CONCLUSION

We investigated the resonant dynamics of hybrid antiskyrmions that emerged at room temperature in  $(\text{Fe}_{0.60}\text{Ni}_{0.32}\text{Pd}_{0.08})_3\text{P}$  by microwave absorption measurement and micromagnetic simulation. A pair of gyrotropic resonant modes is observed, and found to be accompanied by the in-plane propagating spin wave. Such complex dynamics in the hybrid antiskyrmion strings is significantly affected by the Bloch points associated with their hybrid structure. The modulation in the hybrid antiskyrmion spin texture driven by microwave excitation has a potential to provide novel high-frequency spintronics functionalities.

#### ACKNOWLEDGMENTS

We thank N. Nagaosa, F. S. Yasin, and M. Mochizuki for fruitful discussions. D.N. thanks K. Nakajima and RIKEN CEMS Emergent Matter Science Research Support Team for technical assistance. This work was financially supported by JST CREST (Grants No. JPMJCR20T1 and No. JPMJCR1874) and JSPS Grants-in-Aid for Scientific Research (Grants No. 20K15164 and No. 23H01841).

- 
- [1] N. Nagaosa and Y. Tokura, Topological properties and dynamics of magnetic skyrmions, *Nat. Nanotechnol.* **8**, 899 (2013).
  - [2] Y. Tokura and N. Kanazawa, Magnetic skyrmion materials, *Chem. Rev.* **121**, 2857 (2021).
  - [3] A. Fert, N. Reyren, and V. Cros, Magnetic skyrmions: Advances in physics and potential applications, *Nat. Rev. Mater.* **2**, 17031 (2017).
  - [4] K. Everschor-Sitte, J. Masell, R. M. Reeve, and M. Kläui, Perspective: Magnetic skyrmions—Overview of recent progress in an active research field, *J. Appl. Phys.* **124**, 240901 (2018).
  - [5] S. Mühlbauer, B. Binz, F. Jonietz, C. Pfleiderer, A. Rosch, A. Neubauer, R. Georgii, and P. Böni, Skyrmion lattice in a chiral magnet, *Science* **323**, 915 (2009).
  - [6] X. Z. Yu, Y. Onose, N. Kanazawa, J. H. Park, J. H. Han, Y. Matsui, N. Nagaosa, and Y. Tokura, Real-space observation of a two-dimensional skyrmion crystal, *Nature (London)* **465**, 901 (2010).
  - [7] I. Kézsmárki *et al.*, Néel-type skyrmion lattice with confined orientation in the polar magnetic semiconductor  $\text{GaV}_4\text{S}_8$ , *Nat. Mater.* **14**, 1116 (2015).
  - [8] T. Okubo, S. Chung, and H. Kawamura, Multiple- $q$  states and the skyrmion lattice of the triangular-lattice Heisenberg antiferromagnet under magnetic fields, *Phys. Rev. Lett.* **108**, 017206 (2012).
  - [9] W. Koshibae and N. Nagaosa, Theory of antiskyrmions in magnets, *Nat. Commun.* **7**, 10542 (2016).
  - [10] L. Camosi, N. Rougemaille, O. Fruchart, J. Vogel, and S. Rohart, Micromagnetics of antiskyrmions in ultrathin films, *Phys. Rev. B* **97**, 134404 (2018).
  - [11] S. Huang, C. Zhou, G. Chen, H. Shen, A. K. Schmid, K. Liu, and Y. Wu, Stabilization and current-induced motion of antiskyrmion in the presence of anisotropic Dzyaloshinskii-Moriya interaction, *Phys. Rev. B* **96**, 144412 (2017).
  - [12] M. Hoffmann, B. Zimmermann, G. P. Müller, D. Schürhoff, N. S. Kiselev, C. Melcher, and S. Blügel, Antiskyrmions stabilized at interfaces by anisotropic Dzyaloshinskii-Moriya interactions, *Nat. Commun.* **8**, 308 (2017).
  - [13] A. K. Nayak, V. Kumar, T. Ma, P. Werner, E. Pippel, R. Sahoo, F. Damay, U. K. Röbler, C. Felser, and S. S. P. Parkin, Magnetic antiskyrmions above room temperature in tetragonal Heusler materials, *Nature (London)* **548**, 561 (2017).
  - [14] K. Karube, L. Peng, J. Masell, X. Yu, F. Kagawa, Y. Tokura, and Y. Taguchi, Room-temperature antiskyrmions and sawtooth surface textures in a non-centrosymmetric magnet with  $S_4$  symmetry, *Nat. Mater.* **20**, 335 (2021).
  - [15] M. Heigl *et al.*, Dipolar-stabilized first and second-order antiskyrmions in ferrimagnetic multilayers, *Nat. Commun.* **12**, 2611 (2021).
  - [16] X. Z. Yu, N. Kanazawa, W. Z. Zhang, T. Nagai, T. Hara, K. Kimoto, Y. Matsui, Y. Onose, and Y. Tokura, Skyrmion flow near room temperature in an ultralow current density, *Nat. Commun.* **3**, 988 (2012).

- [17] W. Jiang *et al.*, Direct observation of the skyrmion Hall effect, *Nat. Phys.* **13**, 162 (2017).
- [18] L. Peng, K. Karube, Y. Taguchi, N. Nagaosa, Y. Tokura, and X. Yu, Dynamic transition of current-driven single-skyrmion motion in a room-temperature chiral-lattice magnet, *Nat. Commun.* **12**, 6797 (2021).
- [19] M. Mochizuki, Spin-wave modes and their intense excitation effects in skyrmion crystals, *Phys. Rev. Lett.* **108**, 017601 (2012).
- [20] Y. Onose, Y. Okamura, S. Seki, S. Ishiwata, and Y. Tokura, Observation of magnetic excitations of skyrmion crystal in a helimagnetic insulator  $\text{Cu}_2\text{OSeO}_3$ , *Phys. Rev. Lett.* **109**, 037603 (2012).
- [21] T. Schwarze, J. Waizner, M. Garst, A. Bauer, I. Stasinopoulos, H. Berger, C. Pfleiderer, and D. Grundler, Universal helimagnon and skyrmion excitations in metallic, semiconducting and insulating chiral magnets, *Nat. Mater.* **14**, 478 (2015).
- [22] S. Khan, O. Lee, T. Dion, C. W. Zollitsch, S. Seki, Y. Tokura, J. D. Breeze, and H. Kurebayashi, Coupling microwave photons to topological spin textures in  $\text{Cu}_2\text{OSeO}_3$ , *Phys. Rev. B* **104**, L100402 (2021).
- [23] B. Satywali, V. P. Kravchuk, L. Pan, M. Raju, S. He, F. Ma, A. P. Petrović, M. Garst, and C. Panagopoulos, Microwave resonances of magnetic skyrmions in thin film multilayers, *Nat. Commun.* **12**, 1909 (2021).
- [24] R. Takagi, M. Garst, J. Sahliger, C. H. Back, Y. Tokura, and S. Seki, Hybridized magnon modes in the quenched skyrmion crystal, *Phys. Rev. B* **104**, 144410 (2021).
- [25] O. Lee, J. Sahliger, A. Aqeel, S. Khan, S. Seki, H. Kurebayashi, and C. H. Back, Tunable gigahertz dynamics of low-temperature skyrmion lattice in a chiral magnet, *J. Phys.: Condens. Matter* **34**, 095801 (2022).
- [26] D. M. Burn, S. L. Zhang, G. Van Der Laan, and T. Hesjedal, Time-resolved measurement of spin excitations in  $\text{Cu}_2\text{OSeO}_3$ , *Phys. Rev. B* **106**, 174409 (2022).
- [27] Y. Okamura, F. Kagawa, M. Mochizuki, M. Kubota, S. Seki, S. Ishiwata, M. Kawasaki, Y. Onose, and Y. Tokura, Microwave magnetoelectric effect via skyrmion resonance modes in a helimagnetic multiferroic, *Nat. Commun.* **4**, 2391 (2013).
- [28] D. Ehlers, I. Stasinopoulos, V. Tsurkan, H. A. Krug von Nidda, T. Fehér, A. Leonov, I. Kézsmárki, D. Grundler, and A. Loidl, Skyrmion dynamics under uniaxial anisotropy, *Phys. Rev. B* **94**, 014406 (2016).
- [29] Y. Okamura, F. Kagawa, S. Seki, M. Kubota, M. Kawasaki, and Y. Tokura, Microwave magnetochiral dichroism in the chiral-lattice magnet  $\text{Cu}_2\text{OSeO}_3$ , *Phys. Rev. Lett.* **114**, 197202 (2015).
- [30] S. A. Montoya *et al.*, Resonant properties of dipole skyrmions in amorphous Fe/Gd multilayers, *Phys. Rev. B* **95**, 224405 (2017).
- [31] I. Stasinopoulos, S. Weichselbaumer, A. Bauer, J. Waizner, H. Berger, S. Maendl, M. Garst, C. Pfleiderer, and D. Grundler, Low spin wave damping in the insulating chiral magnet  $\text{Cu}_2\text{OSeO}_3$ , *Appl. Phys. Lett.* **111**, 032408 (2017).
- [32] I. Stasinopoulos, S. Weichselbaumer, A. Bauer, J. Waizner, H. Berger, M. Garst, C. Pfleiderer, and D. Grundler, Linearly polarized GHz magnetization dynamics of spin helix modes in the ferrimagnetic insulator  $\text{Cu}_2\text{OSeO}_3$ , *Sci. Rep.* **7**, 7037 (2017).
- [33] S. Seki, M. Garst, J. Waizner, R. Takagi, N. D. Khanh, Y. Okamura, K. Kondou, F. Kagawa, Y. Otani, and Y. Tokura, Propagation dynamics of spin excitations along skyrmion strings, *Nat. Commun.* **11**, 256 (2020).
- [34] M. Weiler, A. Aqeel, M. Mostovoy, A. Leonov, S. Geprägs, R. Gross, H. Huebl, T. T. M. Palstra, and S. T. B. Goennenwein, Helimagnon resonances in an intrinsic chiral magnonic crystal, *Phys. Rev. Lett.* **119**, 237204 (2017).
- [35] S. Pöllath, A. Aqeel, A. Bauer, C. Luo, H. Ryll, F. Radu, C. Pfleiderer, G. Woltersdorf, and C. H. Back, Ferromagnetic resonance with magnetic phase selectivity by means of resonant elastic x-ray scattering on a chiral magnet, *Phys. Rev. Lett.* **123**, 167201 (2019).
- [36] A. Aqeel, J. Sahliger, T. Taniguchi, S. Mändl, D. Mettus, H. Berger, A. Bauer, M. Garst, C. Pfleiderer, and C. H. Back, Microwave spectroscopy of the low-temperature skyrmion state in  $\text{Cu}_2\text{OSeO}_3$ , *Phys. Rev. Lett.* **126**, 017202 (2021).
- [37] X. J. Liu, L. Guo, H. Wang, and Z. K. Tang, The internal dynamic modes of an antiskyrmion in ultrathin ferromagnetic nanodisks, *AIP Adv.* **10**, 075222 (2020).
- [38] L. Peng, K. V. Iakubovskii, K. Karube, Y. Taguchi, Y. Tokura, and X. Yu, Formation and control of zero-field antiskyrmions in confining geometries, *Adv. Sci.* **9**, 2202950 (2022).
- [39] F. S. Yasin *et al.*, Bloch point quadrupole constituting hybrid topological strings revealed with electron holographic vector field tomography, *Adv. Mater.* **36**, 2311737 (2024).
- [40] K. Karube, L. Peng, J. Masell, M. Hemmida, H.-A. K. von Nidda, I. Kézsmárki, X. Yu, Y. Tokura, and Y. Taguchi, Doping control of magnetic anisotropy for stable antiskyrmion formation in schreibersite  $(\text{Fe}, \text{Ni})_3\text{P}$  with  $S_4$  symmetry, *Adv. Mater.* **34**, 2108770 (2022).
- [41] See Supplemental Material at <http://link.aps.org/supplemental/10.1103/PhysRevB.110.024418> for details on experimental setup, additional magnetic resonance data, and numerical analysis of the resonant dynamics.
- [42] D. Nakamura, K. Karube, K. Matsuura, F. Kagawa, X. Yu, Y. Tokura, and Y. Taguchi, Transport signatures of magnetic texture evolution in a microfabricated thin plate of antiskyrmion-hosting  $(\text{Fe}, \text{Ni}, \text{Pd})_3\text{P}$ , *Phys. Rev. B* **108**, 104403 (2023).
- [43] A. Vansteenkiste, J. Leliaert, M. Dvornik, M. Helsen, F. Garcia-Sanchez, and B. Van Waeyenberge, The design and verification of MuMax3, *AIP Adv.* **4**, 107133 (2014).
- [44] S. Seki, M. Suzuki, M. Ishibashi, R. Takagi, N. D. Khanh, Y. Shiota, K. Shibata, W. Koshibae, Y. Tokura, and T. Ono, Direct visualization of the three-dimensional shape of skyrmion strings in a noncentrosymmetric magnet, *Nat. Mater.* **21**, 181 (2022).
- [45] M. T. Birch *et al.*, Toggle-like current-induced Bloch point dynamics of 3D skyrmion strings in a room temperature nanowire, *Nat. Commun.* **13**, 3630 (2022).
- [46] X. Yu, K. V. Iakubovskii, F. S. Yasin, L. Peng, K. Nakajima, S. Schneider, K. Karube, T. Arima, Y. Taguchi, and Y. Tokura, Real-space observations of three-dimensional antiskyrmions and skyrmion strings, *Nano Lett.* **22**, 9358 (2022).
- [47] K. Wagner, A. Kákay, K. Schultheiss, A. Henschke, T. Sebastian, and H. Schultheiss, Magnetic domain walls as reconfigurable spin-wave nanochannels, *Nat. Nanotechnol.* **11**, 432 (2016).